

# Evolution of the Electronic and Excitonic Properties in 2D Ruddlesden-Popper Perovskites Induced by Bifunctional Ligands

Xinjue Zhong<sup>1,\*</sup>, Xiaojuan Ni<sup>2</sup>, Alan Kaplan<sup>1</sup>, Xiaoming Zhao<sup>3</sup>, Marko Ivancevic<sup>3</sup>, Melissa L. Ball<sup>4</sup>, Zhaojian Xu<sup>1</sup>, Hong Li<sup>2</sup>, Barry P Rand<sup>1,4</sup>, Yueh-Lin Loo<sup>3,4</sup>, Jean-Luc Brédas<sup>2</sup>, and Antoine Kahn<sup>1,\*</sup>

<sup>1</sup> Department of Electrical and Computer Engineering, Princeton University, Princeton, NJ, 08544, United States of America.

<sup>2</sup> Department of Chemistry and Biochemistry, The University of Arizona, Tucson, Arizona, 85721-0041, United States of America.

<sup>3</sup> Department of Chemical and Biological Engineering, Princeton University, Princeton, New Jersey 08544, United States of America.

<sup>4</sup> Andlinger Center for Energy and the Environment, Princeton University, Princeton, New Jersey 08544, United States of America.

Corresponding author \*: Antoine Kahn [kahn@princeton.edu](mailto:kahn@princeton.edu)  
Xinjue Zhong [xinjuez@princeton.edu](mailto:xinjuez@princeton.edu)

## Keywords

2D perovskites, bifunctional organic ligands, electronic gap, exciton binding energy

## Abstract

Two-dimensional (2D) Ruddlesden–Popper metal-halide perovskites exhibit structural diversity due to a variety of choices of organic ligands. Incorporating bifunctional ligands in such materials is particularly intriguing since it can result in novel electronic properties and functions. However, an in-depth understanding of the effects of bifunctional ligands on perovskite structures and, consequently, their electronic and excitonic properties, is still lacking. Here,  $n=1$  2D perovskites built with organic ligands containing -CN, -OH, -COOH, -phenyl (Ph), and -CH<sub>3</sub> functional groups are investigated using ultraviolet and inverse photoemission spectroscopies, density functional theory (DFT) calculations, and tight-binding (TB) model analyses. The experimentally determined electronic gaps of the -CN, -COOH, -Ph, and -CH<sub>3</sub> based perovskites exhibit a strong correlation

with the in-plane Pb-I-Pb bond angle, while the -OH based perovskite deviates from the linear trend. Based on the band structure calculations, this anomaly is attributed to the out-of-plane dispersion, caused predominantly by significant interlayer electronic coupling that is present in -OH based perovskites. These results highlight the complex and diverse impacts of organic ligands on electronic properties, especially in terms of the involvement of strong interlayer electronic coupling. The impact of the bifunctional ligands on the evolution of the exciton binding energy is also addressed.

## 1. Introduction

Hybrid organic-inorganic perovskites are among the most promising materials for thin film photovoltaic applications, with single-cell power-conversion efficiency (PCE) reaching 26%.<sup>[1-4]</sup> Yet, achieving long-term device stability remains elusive.<sup>[5-8]</sup> Two-dimensional (2D) hybrid perovskites exhibit enhanced stability with respect to their 3D counterparts, due in part to the bulky organic cations that separate the inorganic metal-halide layers and provide barriers against moisture and other deleterious elements.<sup>[9-12]</sup> The typical formula for (quasi-)2D perovskites is  $A'_m A_{n-1} B_n X_{3n+1}$ , where  $A'$  can be either a monovalent cation ( $m = 2$ ) giving rise to the Ruddlesden-Popper phase<sup>[13]</sup> or a divalent cation ( $m = 1$ ) leading to the Dion-Jacobson phase,<sup>[14]</sup>  $n$  represents the number of metal-halide inorganic layers sandwiched between organic spacers;  $B$  denotes a divalent metal cation and  $X$ , a halogen anion. A wide choice of organic cations  $A'$  provides high chemical and structural tunability, which in turn affects the optical, electronic, and excitonic properties of the material. Such flexibility provides opportunities for fundamental research on structure-properties relationships<sup>[15]</sup> and various applications in light-emitting<sup>[16-18]</sup> and light-harvesting devices.<sup>[13,19]</sup>

The design of 2D perovskite-based devices with specific properties requires a good understanding of the effect that bulky organic cations have on the optoelectronic parameters of the 2D materials, such as frontier energy level positions, electronic and optical gaps, and exciton properties. 2D perovskites form quantum well structures in which the metal-halide octahedra typically constitute the well, owing to the larger molecular energy gap of the separating organic cation, i.e., the energy gap between their highest occupied and lowest unoccupied molecular orbitals (HOMO-LUMO gap). While these organic cations do not directly contribute to the band edges of 2D perovskites, the organic-inorganic interactions can modify the structure of the inorganic framework, including

the B-X-B bond angle<sup>[20,21]</sup> and X-B bond length,<sup>[22]</sup> distort the alignment of the B-X octahedra and affect the interlayer distance.<sup>[23]</sup> These parameters in turn tune the optoelectronic properties of the 2D perovskites. It is therefore important to manipulate the organic-inorganic interactions to examine these effects and learn how to exploit them to tune material properties.

Bifunctional ligands in which the non-ammonium terminus contains a functional group capable of forming extra bonding patterns within the organic bilayer have been introduced into 2D perovskites as an effective means of altering the organic-inorganic interactions.<sup>[11,24,25]</sup> These additional bonds, often hydrogen or halogen bonds,<sup>[26]</sup> modify the interactions between the ammonium terminus of the ligands and the halide ions of the inorganic octahedra, and thus the octahedral tilting and B-X-B angles. A number of bifunctional ligands, such as ethanolammonium (OH-(CH<sub>2</sub>)<sub>2</sub>-NH<sub>3</sub><sup>+</sup>),<sup>[27]</sup> 5-ammonium valeric acid (COOH-(CH<sub>2</sub>)<sub>5</sub>-NH<sub>3</sub><sup>+</sup>),<sup>[28]</sup> and halogen-substituted cations (Cl-(CH<sub>2</sub>)<sub>2</sub>-NH<sub>3</sub><sup>+</sup>, Br-(CH<sub>2</sub>)<sub>2</sub>-NH<sub>3</sub><sup>+</sup>),<sup>[24]</sup> have been synthesized, allowing the exploration of the structure-properties relationship in 2D perovskites. This is exemplified by a recent work by Zhao et al.<sup>[25]</sup> on a series of single-crystalline Ruddlesden-Popper structures containing ligands with cyano,<sup>[29]</sup> alcohol,<sup>[27]</sup> or carboxylic acid<sup>[30]</sup> functionalities. The structure-property analysis reveals a strong dependence of the Pb-I-Pb angle, optical gap, and in-plane mobility on the intermolecular interactions induced by these bifunctional ligands defined in terms of charge separation descriptor (CSD). However, the impact of the bifunctional ligands on the position of frontier energy levels and the electronic gap (E<sub>EG</sub>) of thin films, a frequently used device metric on a format more device relevant, i.e. thin films as opposed to single crystals, has not yet been experimentally investigated. Similarly, another key optoelectronic characteristics of these materials, i.e. the exciton binding energy (E<sub>b</sub>), which can be as high as a few hundred meV for small *n*, needs to be investigated.<sup>[31,32]</sup> Dielectric confinement also plays a vital role in these low-dimensional systems, owing to the large difference between the dielectric constants of the organic layers and the inorganic sheets. The additional functional groups in bifunctional ligands give a means of tuning the dielectric confinement and, consequently, the exciton binding energy.

In the present study, we perform ultraviolet photoelectron spectroscopy (UPS) and inverse photoemission spectroscopy (IPES) measurements, combined with X-ray diffraction (XRD) and optical absorption measurements on thin films of the *n* = 1 2D perovskite (CN-EA)<sub>2</sub>PbI<sub>4</sub>, (OH-EA)<sub>2</sub>PbI<sub>4</sub>, (COOH-PA)<sub>2</sub>PbI<sub>4</sub>, (Ph-EA)<sub>2</sub>PbI<sub>4</sub>, and (CH<sub>3</sub>-PA)<sub>2</sub>PbI<sub>4</sub> (where Ph = phenyl group, PA =

propylammonium, and EA= ethyl ammonium). The chemical structures of these bifunctional ligands are shown in Figure 1a. In the organic layer, the (CN-EA)<sup>+</sup>, (OH-EA)<sup>+</sup>, and (COOH-PA)<sup>+</sup> cations exhibit strong hydrogen-bonding interactions whereas the (Ph-EA)<sup>+</sup> cations are held together through  $\pi$ - $\pi$  interactions. (CH<sub>3</sub>-PA)<sup>+</sup> is included as a reference since these cations interact primarily via (weak) van der Waals interactions. Different intermolecular interactions within the organic bilayer induce distinct organic-inorganic interactions leading to octahedral tilting and distortion of Pb-I-Pb angles, which allows for investigations of the relationship between structure and electronic properties. We determine the electronic properties, namely the energy positions of the valence band maximum (VBM) and conduction band minimum (CBM), and the electronic, or single-particle, gap of these 2D perovskites, via UPS and IPES. With scanning tunneling spectroscopy (STS), the UPS/IPES combination is unique in providing experimental values of the energy of uncorrelated electron and hole states, and therefore the single particle or electronic gap, in excitonic materials such as molecular or 2D materials.<sup>[32,33]</sup> These values are critical for understanding the energetics of devices that incorporate 2D perovskites. On the structure side, the Pb-I-Pb bond angle is determined through a combination of the experimental analysis of structure files established for single crystals and theoretical calculations based on DFT-optimized crystal structures, assuming the same structures are applicable to our ~200 nm thin films. We show that the electronic gap of (CN-EA)<sub>2</sub>PbI<sub>4</sub>, (COOH-PA)<sub>2</sub>PbI<sub>4</sub>, (Ph-EA)<sub>2</sub>PbI<sub>4</sub>, and (CH<sub>3</sub>-PA)<sub>2</sub>PbI<sub>4</sub> increases as the in-plane Pb-I-Pb bond angle is reduced with respect to its undistorted 180° value, revealing a strong linear correlation with an R<sup>2</sup> value = 0.9390. While UPS / IPES techniques are surface sensitive and probe the first couple of inorganic (Pb-I) planes, Y. Shao et al.<sup>[34]</sup> have shown that the surface structure is closely reproduced in the bulk of the film for *n*=1 2D perovskites. Hence, we make the assumption that the optoelectronic properties experimentally determined here via UPS/IPES carry through the bulk of our films. (OH-EA)<sub>2</sub>PbI<sub>4</sub> exhibits a notable deviation from this trend, with a gap that is approximately 0.25 eV smaller than what would be expected based on the linear trends. This structure-property relationship is further explored using density functional theory (DFT) calculations and tight-binding (TB) model analysis. The calculated gaps closely follow the trend of the experimental results. The smaller electronic gap of (OH-EA)<sub>2</sub>PbI<sub>4</sub> is found at the Z-point rather than at the  $\Gamma$ -point as in the case of the other four materials. A clear electronic dispersion appears in the  $\Gamma$ -Z direction, indicating an overlap between atomic orbitals of adjacent 2D planes and therefore significant interlayer coupling in (OH-EA)<sub>2</sub>PbI<sub>4</sub>. By subtracting the

optical gap ( $E_{OG}$ ) from  $E_{EG}$ , we deduce  $E_b$ , which varies from 360 meV for  $(CH_3-PA)_2PbI_4$  to 70 meV for  $(OH-EA)_2PbI_4$ . This large span is linked to the variety of quantum and dielectric confinement induced by the bifunctional ligands.

## 2. Results and Discussion

All perovskite films were spin-coated on indium tin oxide (ITO) following fabrication procedures given in the Experimental Section and the details provided by Zhao et. al.<sup>[25]</sup> XRD and ultraviolet-visible (UV-Vis) spectroscopy were performed as the first characterization step. XRD traces of all films exhibit dominant (002) or (001) features and their higher-order peaks (Figure 1b), confirming the in-plane layering of the 2D phases. The interlayer spacing for  $(CN-EA)_2PbI_4$ ,  $(OH-EA)_2PbI_4$ ,  $(COOH-PA)_2PbI_4$ ,  $(Ph-EA)_2PbI_4$ , and  $(CH_3-PA)_2PbI_4$  are 1.02 nm, 1.01 nm, 1.21 nm, 1.63 nm, and 1.38 nm, respectively, in good agreement with the structures calculated for single crystals. These interlayer spacings  $d$  were calculated using Bragg's law ( $n \times \lambda = 2 \times d \times \sin\theta$ ), in which the value of  $\theta$  corresponds to the maximum intensity point of each peak in the XRD spectra. To define the accuracy of the interlayer spacing values, we use the angular measurement interval  $\theta$  of  $0.05^\circ$  and perform an error propagation analysis to determine the error on  $d$  (see Section S1 in the SI for details) The presence of (111) and (101) peaks in the  $(CN-EA)_2PbI_4$  spectrum suggests multiple orientations in the films. Although different orientations may impact some measurements on the work function (WF) of the films, this should not affect  $E_{EG}$  or  $E_b$ . The optical absorption spectra (Figure 1c) exhibit a single excitonic peak for each film, which is consistent with the quantum confinement expected for these layered structures. The Elliott formula<sup>[35,36]</sup> was employed to model the absorption near the band edge, identifying the predominant 1s excitonic peak (Figure S1). This approach yields optical gaps ( $E_{OG}$ ), determined by the excitonic peaks, of 2.31 eV, 2.34 eV, 2.41 eV, 2.41 eV, and 2.44 eV for  $(CN-EA)_2PbI_4$ ,  $(OH-EA)_2PbI_4$ ,  $(COOH-PA)_2PbI_4$ ,  $(Ph-EA)_2PbI_4$ , and  $(CH_3-PA)_2PbI_4$ , respectively.

The photoluminescence (PL) spectra (Figure S2) also show a distinct excitonic peak with a small Stokes shift. The excitonic peaks for  $(COOH-PA)_2PbI_4$  and  $(CN-EA)_2PbI_4$  appear broader than the others with full-width at half maximum (FWHM) of 22 nm and 29 nm, respectively. Specifically, the PL of  $(COOH-PA)_2PbI_4$  is more asymmetric and contains a long tail extending to  $\sim 670$  nm below the peak. Asymmetric and broad PL shapes in 2D perovskites have been previously observed and investigated.<sup>[37-39]</sup> The broader emission from  $(CN-EA)_2PbI_4$  is likely attributed to

structural disorders and defects,<sup>[40]</sup> evident from the XRD spectrum, which displays low signal-to-noise ratio and reveals multiple orientations. The exact origin of the low-energy tail in (COOH-PA)<sub>2</sub>PbI<sub>4</sub> remains unclear, though it possibly results from defects and/or exciton-phonon interactions. Ni et al.<sup>[37]</sup> and Motti et al.<sup>[38]</sup> found that the choice of organic cations influences the phonon modes that couple to the excitons in 2D perovskites, subsequently affecting the broadening and asymmetry of PL line shape.

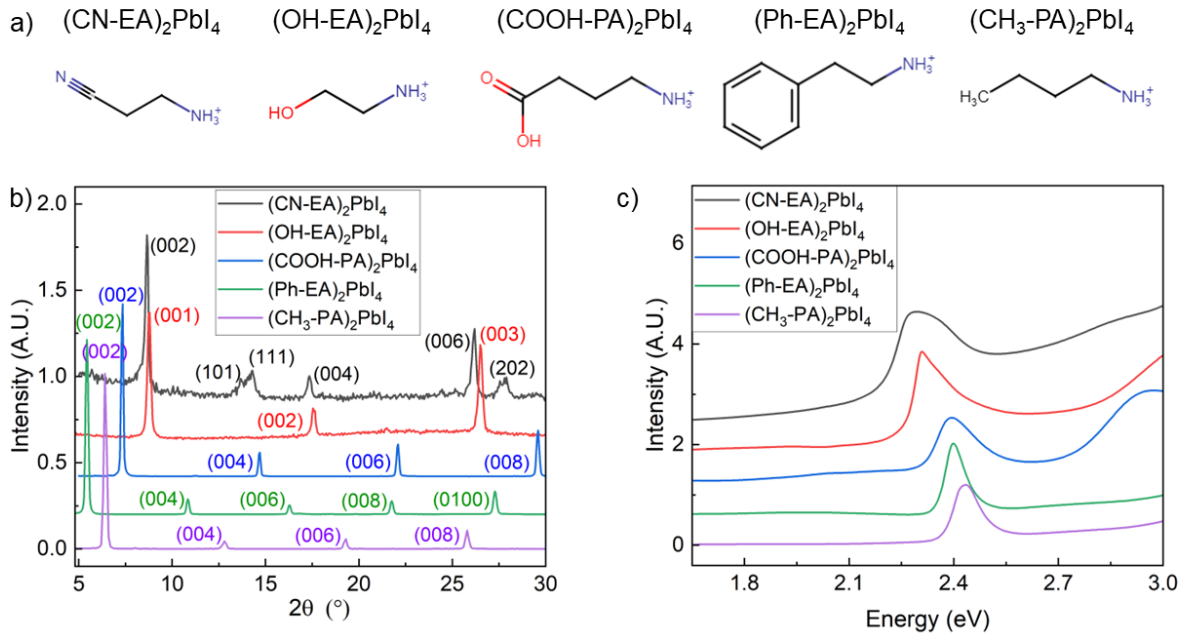


**Figure 1.** a) Chemical structure of bifunctional ligands with functional groups -CN, -OH, -COOH, -Ph, and -CH<sub>3</sub>, respectively. b) XRD spectra of the 2D perovskite thin films, each dominated by the (002) or (001) peak. c) Absorption spectra showing a single excitonic peak for each film. The optical gap is determined by using Elliott formula.

The valence and conduction states of (CN-EA)<sub>2</sub>PbI<sub>4</sub> and (COOH-PA)<sub>2</sub>PbI<sub>4</sub>, measured at room temperature via UPS and IPES in ultrahigh vacuum, are shown in Figure 2a,c. The corresponding energy diagrams are depicted in Figure 2b,d. The spectra for all five perovskites are shown in Figure S3. The VBM of each film is determined at the intersection of the valence spectrum onset and the background (noise level) plotted on a logarithmic scale (Figure S4), following a methodology developed in other metal halide perovskite studies.<sup>[32,41,42]</sup> The CBM is determined by a simple extrapolation of the leading edge of the IPES spectrum, plotted on a linear scale. By combining the position of the VBM and CBM and the WF measured from the secondary photoemission cut-off, we determine the ionization energy (IE), electron affinity (EA), and E<sub>EG</sub> to be 5.86 eV, 3.42 eV, and 2.44 eV for (CN-EA)<sub>2</sub>PbI<sub>4</sub>, and 5.82 eV, 3.15 eV, and 2.67 eV for

(COOH-PA)<sub>2</sub>PbI<sub>4</sub>, respectively. Variations in IE and EA result from a number of factors, including surface composition,<sup>[43]</sup> orbital overlaps caused by the distortion of the inorganic framework (Pb-I-Pb angle),<sup>[20,24]</sup> and surface dipoles induced by the bifunctional ligands.<sup>[44,45]</sup> The electronic gaps derived from the VBM and CBM measurements range from 2.80 eV for (CH<sub>3</sub>-PA)<sub>2</sub>PbI<sub>4</sub> to 2.41 eV for (OH-EA)<sub>2</sub>PbI<sub>4</sub>. The values obtained for (OH-EA)<sub>2</sub>PbI<sub>4</sub> and (Ph-EA)<sub>2</sub>PbI<sub>4</sub> are in good agreement with those measured by the electro-absorption technique used in a recent comprehensive study by Hansen et al.,<sup>[46]</sup> while the gap obtained for (CH<sub>3</sub>-PA)<sub>2</sub>PbI<sub>4</sub> is slightly larger than reported in their study. A summary of all gaps is given in Table S1 and S2, with experimental errors estimated to be about 0.15 eV, based on experimental resolution of the techniques, data analysis procedure and repeatability of the data (Table S1).

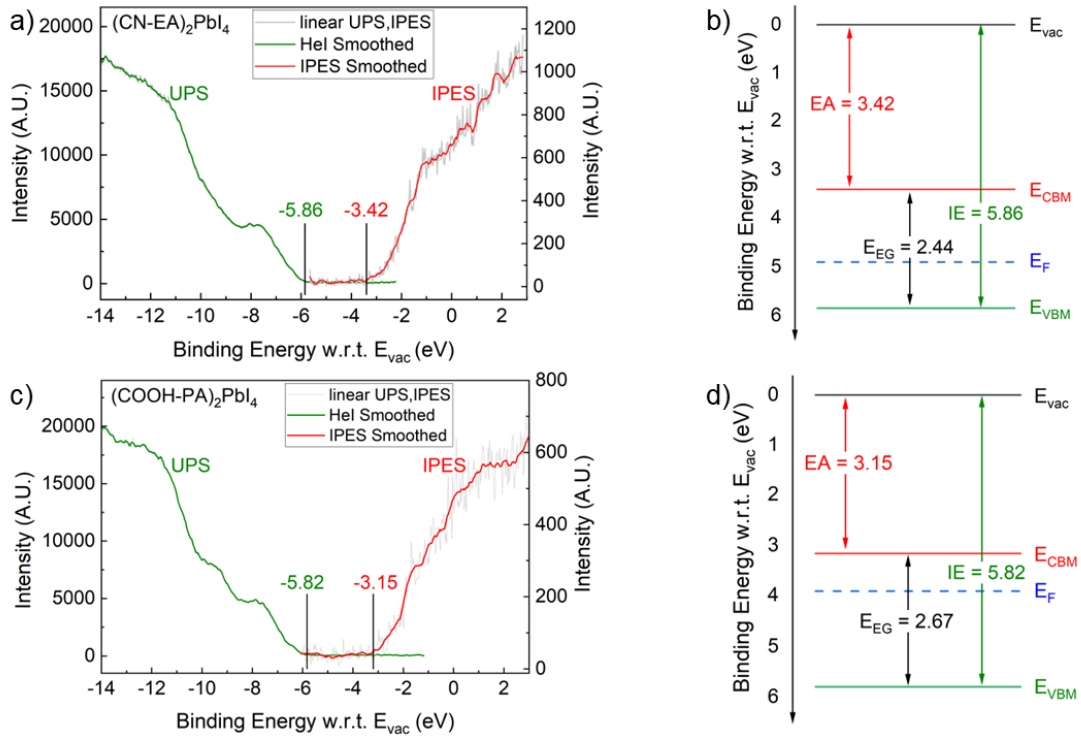


**Figure 2.** a), c) UPS He-I and IPES spectra measured on a) (CN-EA)<sub>2</sub>PbI<sub>4</sub> and c) (COOH-PA)<sub>2</sub>PbI<sub>4</sub>, showing the VBM and CBM positions with respect to the vacuum level ( $E_{vac}$ ). b), d) Corresponding energy diagram with respect to  $E_{vac}$  showing the VBM ( $E_{VBM}$ ) in green, Fermi level ( $E_F$ ) in blue, CBM ( $E_{CBM}$ ) in red, and  $E_{vac}$  in black. Ionization energies (IE), electron affinities (EA), and electronic gaps ( $E_{EG}$ ) are given.

To understand the significant differences in the optical and electronic properties of these 2D materials, we performed DFT calculations to evaluate crystal structures, densities of states, and electronic band structures of these five perovskites, using the Heyd–Scuseria–Ernzerhof (HSE)<sup>[47]</sup> range-separated hybrid functional with 35% Hartree–Fock exchange (HF), and including explicitly the spin–orbit coupling (SOC) effects. Details are given in the Experimental Section. In the optimized crystal structures, the (CN-EA)<sup>+</sup> and (OH-EA)<sup>+</sup> ligands assemble into a pseudo-hexagonal dimer via a pair-wise hydrogen bond between the functional group of one ligand and the ammonium terminus of the other, where the (COOH-PA)<sup>+</sup> ligands form a zipper-shaped chain via hydrogen-bonding interactions across the organic bilayer, which is consistent with previous reports.<sup>[25]</sup> The (Ph-EA)<sup>+</sup> ligands adopt a face-to-edge configuration between the two organic layers and the aromatic rings of the ligands are parallel within each layer due to  $\pi$ - $\pi$  interactions.<sup>[21]</sup> Details on the calculated 2D perovskite structures are shown in Figure S6. These differences in intermolecular interactions directly affect the interactions between hydrogens in the ammonium groups and iodine atoms in the octahedra, and, thus, the assembly of the inorganic framework, as shown in Figure 3. The calculated in-plane Pb-I-Pb angle decreases from 176° for (CN-EA)<sub>2</sub>PbI<sub>4</sub> to 145° for (CH<sub>3</sub>-PA)<sub>2</sub>PbI<sub>4</sub>, which agrees well with the experimental Pb-I-Pb angles derived from crystal structures (Figure S7).<sup>[21,25,27]</sup> The out-of-plane Pb-I bond of the (CN-EA)<sub>2</sub>PbI<sub>4</sub> octahedra remains nearly perpendicular to the 2D plane, while the out-of-plane tilting is more significant in (CH<sub>3</sub>-PA)<sub>2</sub>PbI<sub>4</sub>.

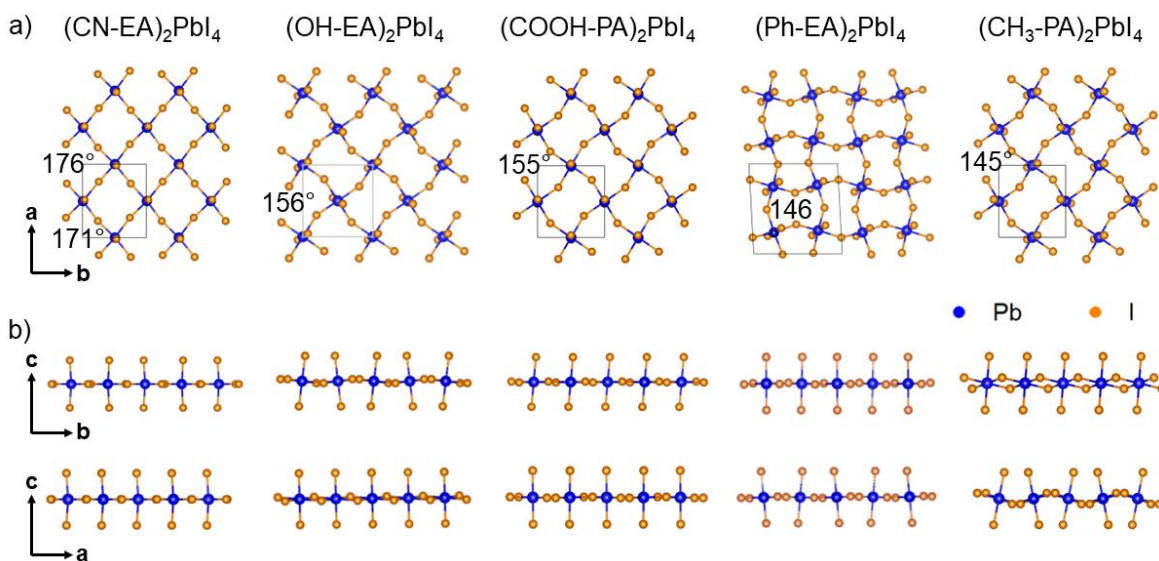


**Figure 3.** Schematic of a layer of the inorganic framework in a) top view and b) side view, showing the in-plane Pb-I-Pb angle and out-of-plane distortions.

The analysis of the structure-property relationship for this series of 2D perovskites reveals a strong linear relationship between the experimentally determined electronic gaps of  $(\text{CN-EA})_2\text{PbI}_4$ ,  $(\text{COOH-PA})_2\text{PbI}_4$ ,  $(\text{Ph-EA})_2\text{PbI}_4$ , and  $(\text{CH}_3\text{-PA})_2\text{PbI}_4$  and the corresponding calculated Pb-I-Pb angles, with a remarkable correlation factor  $R^2 = 0.9390$  (Figure 4a). The electronic gap drops from 2.80 eV for  $(\text{CH}_3\text{-PA})_2\text{PbI}_4$  with a Pb-I-Pb angle of  $145^\circ$  to 2.44 eV for  $(\text{CN-EA})_2\text{PbI}_4$  with a Pb-I-Pb angle close to  $180^\circ$ . The optical gaps derived from Elliott formula exhibits a linear relationship with the calculated Pb-I-Pb angle ( $R^2 = 0.9309$  and  $0.9592$ , respectively), which agrees with previous reports.<sup>[21,25]</sup> We note that the electronic gaps calculated at the HSE-SOC level (with 35% HF exchange) follow the trend observed for the experimental gaps as a function of the Pb-I-Pb angle ( $R^2 = 0.8389$ ), although the values are underestimated by  $\approx 0.4$  eV. This correlation is further confirmed by examining the relationship between the gaps and the experimental Pb-I-Pb angle, shown in Figure S5. The variation in the electronic gap is mainly related to the Pb and I orbital overlap, given that the VBM and CBM are dominated by Pb(6s)-I(5p) mixed states and Pb(6p) orbitals, respectively, as demonstrated by the projected densities of states (PDOS) shown in Figure S8. By bending the Pb-I-Pb bond angle away from the ideal  $180^\circ$ , the Pb s- and I p-orbital overlap is reduced, resulting in a decrease in electronic bandwidths and an increase in electronic gap.

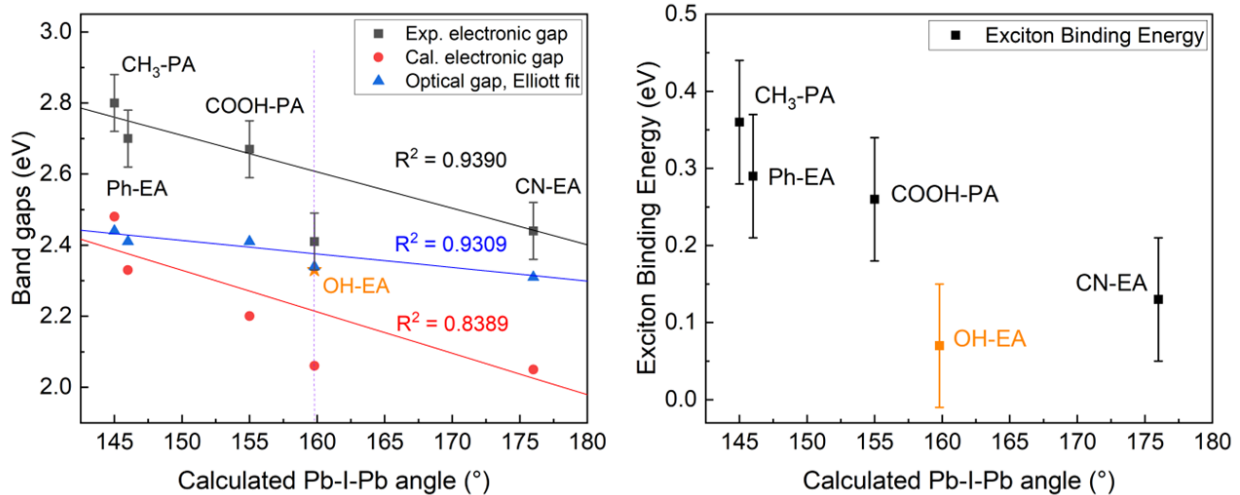


**Figure 4.** a) Electronic and optical gaps vs. calculated Pb-I-Pb angle. Experimental electronic gaps in black; calculated electronic gaps in red; optical gaps in blue; the calculated bandgap at the  $\Gamma$  point of  $(\text{OH-EA})_2\text{PbI}_4$  is also given in orange with a star mark for reference; values for  $(\text{OH-EA})_2\text{PbI}_4$  highlighted by the purple dotted line. The error bar for the experimental electronic gaps is added. b) Experimentally determined exciton binding energy of the five 2D perovskites.

Interestingly, both experimental and calculated electronic gaps of  $(\text{OH-EA})_2\text{PbI}_4$  deviate from the linear trend, with values  $\approx 0.25$  eV smaller than what would be predicted from the linear evolutions. To understand this anomaly, we examined in detail the band structures calculated at the HSE–SOC level for the five 2D perovskites. We find that in contrast to  $(\text{COOH-PA})_2\text{PbI}_4$ ,  $(\text{Ph-EA})_2\text{PbI}_4$ , and  $(\text{CH}_3\text{-PA})_2\text{PbI}_4$ , for which the valence and conduction bands in the  $\Gamma$ -Z direction are nearly flat and point to the absence of any electronic communication between inorganic layers, the valence band in  $(\text{OH-EA})_2\text{PbI}_4$  and  $(\text{CN-EA})_2\text{PbI}_4$  exhibits some dispersion along the  $\Gamma$ -Z direction. In particular, the band dispersion along the  $\Gamma$ -Z direction for  $(\text{OH-EA})_2\text{PbI}_4$  is  $\sim 0.2$  eV, which indicates a significant electronic coupling between adjacent inorganic layers. This is further confirmed by the partial charge densities at the Z point for the VBM of  $(\text{OH-EA})_2\text{PbI}_4$  (Figure S10), which are strongly delocalized within the inorganic layers. The strong interlayer electronic coupling is associated with the shortest I–I distance between two adjacent layers, 4.16 Å for  $(\text{OH-EA})_2\text{PbI}_4$  and 4.44 Å for  $(\text{CN-EA})_2\text{PbI}_4$  (summary is given in Table S4), respectively, as previously observed in Dion-Jacobson perovskites.<sup>[33]</sup> We also note that, unlike the other four perovskites, the VBM and CBM of  $(\text{OH-EA})_2\text{PbI}_4$  locate at the Z point rather than at the  $\Gamma$  point (Figure 5a-e). Remarkably, the calculated gap at the  $\Gamma$  point for  $(\text{OH-EA})_2\text{PbI}_4$  is 2.33 eV (orange star in Figure 4a), a value that matches well the linear trend of the calculated electronic gaps. This implies that, while angle-integrated UPS/IPES measurements done here cannot access the gap at the  $\Gamma$  point, theory can, and identifies the electronic gap in accord with the Pb-I-Pb distortion in the material. To elucidate the distinctive location of the band gap in  $(\text{OH-EA})_2\text{PbI}_4$ , we conducted an additional tight-binding model analysis, focusing on the impact of interlayer coupling on the electronic band dispersion along the  $\Gamma$ -Z direction in layered perovskites. Our analysis reveals that the out-of-plane electron hopping integral exhibits a positive sign for  $(\text{OH-EA})_2\text{PbI}_4$ , supporting the crucial role of interlayer coupling in shaping the band dispersion from Z to  $\Gamma$ . Details are provided in the SI (Figures S11 and S12). These findings suggest that the electronic bandgap of  $(\text{OH-EA})_2\text{PbI}_4$  is dominated by the out-of-plane interactions rather than the in-plane orbital overlaps, thus highlighting its deviation from the linear trend observed in the other four perovskites.

We further investigated the impact of the functional group of the organic cations on the exciton binding energy  $E_b$  obtained by subtraction of the experimental  $E_{\text{OG}}$  derived from Elliott formula from the experimental  $E_{\text{EG}}$ .  $E_b$  is found to decrease monotonously with increasing Pb-I-Pb angle, from 360 meV for  $(\text{CH}_3\text{-PA})_2\text{PbI}_4$  down to 130 meV for  $(\text{CN-EA})_2\text{PbI}_4$ , with an apparently

anomalous value of 70 meV for  $(\text{OH-EA})_2\text{PbI}_4$  (Figure 4b). The  $(\text{Ph-EA})_2\text{PbI}_4$  value (290 meV) falls between  $E_b = 250$  meV from Cheng et al.<sup>[48]</sup> and  $E_b = 370$  meV reported for single crystals by Ishihara et al.<sup>[49]</sup> Our result for  $(\text{OH-EA})_2\text{PbI}_4$  is comparable to the values derived from temperature-dependent PL ( $E_b = 65$  meV)<sup>[50]</sup> and electro-absorption measurements ( $E_b = 55$  meV),<sup>[46]</sup> respectively, but is significantly smaller than the values reported in Figure 4b for the other four systems.

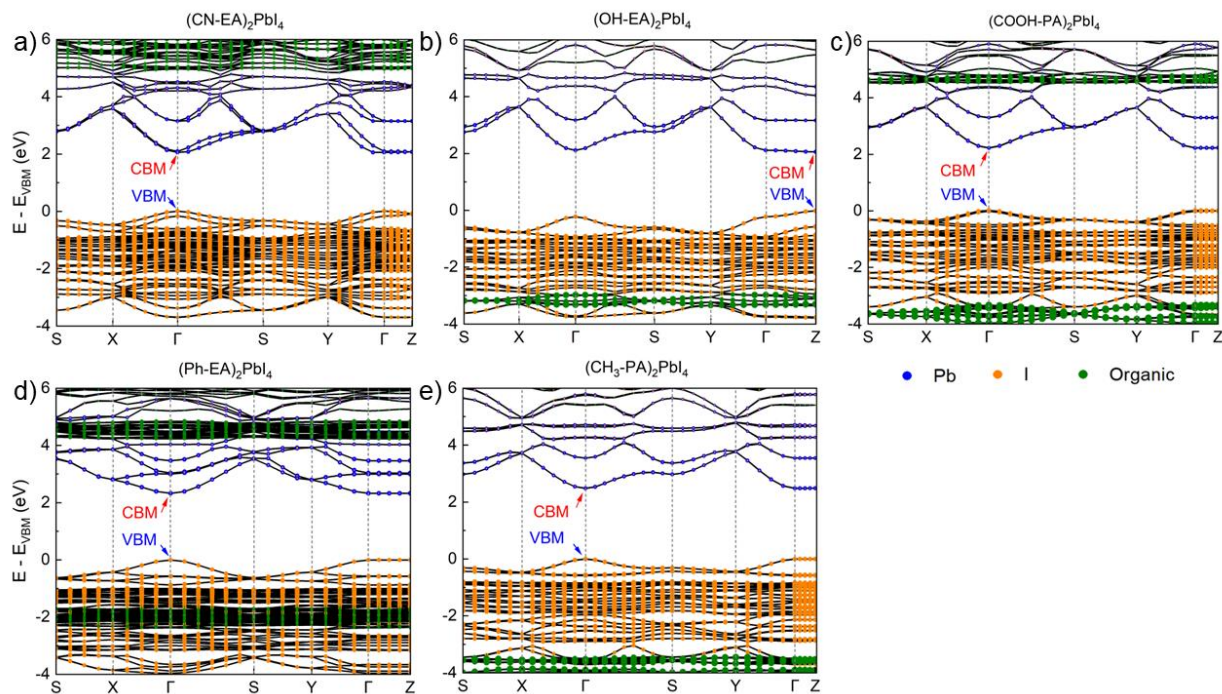


**Figure 5.** Band structure calculated at the HSE–SOC level for a)  $(\text{CN-EA})_2\text{PbI}_4$ , b)  $(\text{OH-EA})_2\text{PbI}_4$ , c)  $(\text{COOH-PA})_2\text{PbI}_4$ , d)  $(\text{Ph-EA})_2\text{PbI}_4$  and e)  $(\text{CH}_3\text{-PA})_2\text{PbI}_4$ . The coordinates of the high-symmetry k-points along which the band structures were calculated are provided in Figure S9 and Table S3.

Excitons in these 2D perovskite films live in the inorganic Pb-I well. The HOMO-LUMO gap of the organic cation is significantly larger than that of the inorganic layer (Figure S8), and forms with it a type-I quantum-well structure that confines the exciton to the 2D plane. The variations in the  $E_b$  result therefore in part from the changes in the structure of the inorganic plane. As the Pb-I-Pb bond angle decreases from  $(\text{CN-EA})_2\text{PbI}_4$  to  $(\text{CH}_3\text{-PA})_2\text{PbI}_4$ , the overlap between the Pb 5s and I 5p orbitals is reduced, resulting in greater electronic confinement and a larger bandgap and exciton binding energy. Naturally, this trend is only valid within the same inorganic framework, namely  $[\text{PbI}_4]^{2-}$ , in this series of materials, and would not necessarily be expected to hold upon changing or mixing the metal or halogen species. Hansen et al.<sup>[46]</sup> also identify a comparable correlation between  $E_b$  and octahedral tilting angle, attributing it to variations in the

effective mass caused by the tilting angle, which in turn affects  $E_b$ . In addition, organic cations with different functional groups lead to variations in the dielectric constant ( $\epsilon_b$ ) and in the spacing between the inorganic planes, thereby giving rise to distinct dielectric confinement<sup>[51]</sup> and superlattice screening effects.<sup>[46,52]</sup> A higher  $\epsilon_b$  of the organic cation layer generally leads to increased screening in the inorganic well and a concomitant decrease in  $E_b$ . Our results of low  $E_b$  for (OH-EA)<sub>2</sub>PbI<sub>4</sub> and high  $E_b$  for (CH<sub>3</sub>-PA)<sub>2</sub>PbI<sub>4</sub> can be partially attributed to a relatively high  $\epsilon_b$  of ~2.45 in the (OH-EA)<sup>[46]</sup> layer compared to ~1.75 in the (CH<sub>3</sub>-PA) layer. The low  $E_b$  in (OH-EA)<sub>2</sub>PbI<sub>4</sub> also results from the strong interlayer coupling due to the short interlayer spacing of 1.01 nm in (OH-EA)<sub>2</sub>PbI<sub>4</sub>. Excitons in the [PbI<sub>4</sub>]<sup>2-</sup> layer experience partial screening by adjacent inorganic layer, a phenomenon known as superlattice screening.<sup>[46,52]</sup> This screening effect becomes more pronounced as the interlayer spacing decreases. This also explains the significantly different  $E_b$  between (COOH-PA)<sub>2</sub>PbI<sub>4</sub> and (OH-EA)<sub>2</sub>PbI<sub>4</sub> despite their similar in-plane Pb-I-Pb angles and comparable dielectric constants of the organic ligands. The interlayer spacing and the shortest interlayer I---I distances are 1.01 nm and 4.16 Å, respectively, in the (OH-EA) case, compared to 1.21 nm and 7.13 Å for COOH-PA (see above and Table S4). This larger interlayer spacing in (COOH-PA)<sub>2</sub>PbI<sub>4</sub> functions as an effective barrier that prevents electronic communication between the 2D planes and contributes to higher confinement, thus an increase in electronic gap and exciton binding energy. This confinement of carriers to a single well is consistent with the flat band observed along the  $\Gamma$ -Z direction of the DFT calculated band structures.

### 3. Conclusions

In summary, we have investigated the impact of bifunctional organic ligands on thin-film structures, optoelectronic properties, and excitonic effects. Using a combination of UPS and IPES measurements, optical absorption, and range-separated DFT calculations, we demonstrate that the electronic bandgaps related to in-plane excitons exhibit a strong linear correlation with the in-plane Pb-I-Pb angles, whereas the value of (OH-EA)<sub>2</sub>PbI<sub>4</sub> deviates from the linear trend due to significant interlayer electronic coupling. These results highlight the intricate and diverse impacts of organic ligands on electronic properties, with a specific emphasis on the significant role played by strong interlayer electronic coupling. We further determine the exciton binding energy of each perovskite and demonstrate that its variation originates from the modification in the quantum and

dielectric confinements induced by the functional groups in the organic ligands. **The strong interlayer coupling in (OH-EA)<sub>2</sub>PbI<sub>4</sub> introduces additional superlattice screening effects into the material, which further lowers the exciton binding energy.** These findings provide important insights into the structure-properties relationships in 2D RP perovskites and open the way for designing devices with the desired properties via selecting bifunctional ligands. The strong interlayer electronic coupling, as observed in (OH-EA)<sub>2</sub>PbI<sub>4</sub>, could potentially be utilized for efficient charge transport between adjacent layers, leading to enhanced device performance in 2D perovskite devices.

#### **4. Experimental Section**

##### **Materials**

Ethanolammonium iodide (OH-EAI) and phenethylammonium iodide (PEAI) was purchased from Greatcell Solar Materials, lead iodide (PbI<sub>2</sub>, 99.99%) was purchased from TCI America, and N,N-Dimethylformamide (DMF, >99.8%) was purchased from Acros Organics.

##### **2D perovskite precursor solutions and thin film processing**

All 2D perovskite precursor solutions were prepared and spin-coated in a nitrogen-filled glovebox. PEA<sub>2</sub>PbI<sub>4</sub> and (OH-EA)<sub>2</sub>PbI<sub>4</sub> precursor solutions were prepared by dissolving stoichiometric ammonium salts (i.e., PEA<sup>+</sup>, OH-EA<sup>+</sup>) and PbI<sub>2</sub> in DMF at a concentration of 0.2 M or 0.15 M. (COOH-PA)<sub>2</sub>PbI<sub>4</sub> and (CN-EA)<sub>2</sub>PbI<sub>4</sub> precursor solutions were prepared by dissolving single crystals (described below) in DMF at a concentration of 0.2 M or 0.15 M.

2D perovskite single crystals were synthesized using the procedure described in Zhao et. al.<sup>[25]</sup> 5 mmol PbI<sub>2</sub> were dissolved in 5 mL HI solution with 0.85 mL hypophosphorous acid and heated to 110 °C to get a clear yellow solution. In a separate vial, 10 mmol amines (i.e., COOH-PA, CN-EA) was dissolved with 5 mL HI solution under an ice bath and thereafter this solution was added dropwise into the hot PbI<sub>2</sub> solution with continuous stirring. Once a clear yellow solution was formed, the stir bar was removed from the vial and the vial was put on a programmable hotplate and slowly cooled down from 110 to 40 °C at a rate of 1 °C/h. The obtained single crystals were filtered and washed by copious amount of diethyl ether. Finally, the crystals were put in a vacuum oven at 40 °C overnight to remove residual solvents.

All perovskite thin films were prepared by spin-coating the precursor solution at 3000 rpm for 30 s, with an acceleration rate of 1000 rpm/s. The films were then thermally annealed at 100 °C for 1 h to remove residual solvent, except (OH-EA)<sub>2</sub>PbI<sub>4</sub> which was annealed for 90 minutes.

(OH-EA)<sub>2</sub>PbI<sub>4</sub> films converted to the orange phase after resting overnight in an ambient atmosphere (~30% RH).

**Optical characterization.** UV-vis absorption spectra were measured using an Agilent Technologies Cary 5000 spectrophotometer. PL spectra were obtained with an Edinburgh Instruments FLS980 photoluminescence spectrometer. All measurements were performed in an ambient environment.

**X-ray diffraction (XRD) measurements.** XRD measurements were performed using a Bruker D8 Discover X-ray Diffractometer on thin films deposited on ITO substrates. Spectra were measured between  $2\theta$  between 4° and 30°, with a step of 0.02° and a speed of 5 degrees per minute.

**Ultraviolet and inverse photoemission spectroscopy (UPS/IPES)** UPS and IPES were performed in ultrahigh vacuum ( $10^{-10}$  Torr) at room temperature on thin-film samples that had no ambient exposure. The work function and valence band edges were determined in UPS using He I (21.22 eV) photons. Valence band spectra were recorded on a logarithmic intensity scale and a linear scale, respectively. The conduction band edges were determined in IPES in the same chamber, in the isochromat mode, with electron energies of 5–15 eV onto the sample. The experimental energy resolutions for UPS and IPES are typically 0.10 and 0.45 eV respectively.

#### **DFT calculations.**

Density functional theory (DFT) calculations were carried out using the projector-augmented wave method as implemented in the Vienna Ab initio Simulation Package (VASP).<sup>[53]</sup> The geometry optimizations were performed at the generalized gradient approximation/Perdew-Burke-Ernzerhof (PBE) level with D3 van der Waals corrections.<sup>[54–56]</sup> The crystal structures of the perovskites were optimized by relaxing both lattice parameters and atomic coordinates until the total force on each atom was less than 0.01 eV/Å. The plane-wave cutoff energy was set to 500 eV. A  $\Gamma$ -centered Pack-Monkhorst  $6 \times 6 \times 3$  k-mesh for (CN-EA)<sub>2</sub>PbI<sub>4</sub>, (COOH-PA)<sub>2</sub>PbI<sub>4</sub>, (Ph-EA)<sub>2</sub>PbI<sub>4</sub>, and (CH<sub>3</sub>-PA)<sub>2</sub>PbI<sub>4</sub>, and a  $6 \times 6 \times 5$  k-mesh for (OH-EA)<sub>2</sub>PbI<sub>4</sub> were employed, respectively. The range-separated hybrid functional of Heyd-Scuseria-Ernzerhof (HSE)<sup>[47,57]</sup> with 35% Hartree-Fock

exchange was then considered to calculate the densities of states and electronic band structures with the inclusion of the spin-orbit coupling (SOC) effects. The high-symmetry k-points along which the band structures were calculated are provided in Table S3.

## Supporting Information

### Acknowledgments

Work at Princeton University was supported by the U.S. Department of Energy's Office of Energy Efficiency and Renewable Energy (EERE) under the Solar Energy Technologies Office (SETO) Award No. DE-EE0008560, and by Grant No. 2018349 from the United States-Israel Binational Science Foundation (BSF). Work at the University of Arizona (U of A) was supported by the Office of Naval Research under Award No. N00014-22-1-2379 and by the U of A College of Science. The computing resources were provided by the Research Data Center at the U of A. M.L.B. is supported by a Princeton Presidential Post-doctoral Fellowship. A.B.K. is supported by the National Science Foundation Graduate Research Fellowship Program under Grant No. DGE-2039656.

### Conflict of Interest

The authors declare no conflict of interest.

### References

- [1] H. Li, J. Zhou, L. Tan, M. Li, C. Jiang, S. Wang, X. Zhao, Y. Liu, Y. Zhang, Y. Ye, W. Tress, C. Yi, *Sci. Adv.* **2022**, *8*, eabo7422.
- [2] J. Jeong, M. Kim, J. Seo, H. Lu, P. Ahlawat, A. Mishra, Y. Yang, M. A. Hope, F. T. Eickemeyer, M. Kim, Y. J. Yoon, I. W. Choi, B. P. Darwich, S. J. Choi, Y. Jo, J. H. Lee, B. Walker, S. M. Zakeeruddin, L. Emsley, U. Rothlisberger, A. Hagfeldt, D. S. Kim, M. Grätzel, J. Y. Kim, *Nature* **2021**, *592*, 381.
- [3] J. Chen, Y. Yang, H. Dong, J. Li, X. Zhu, J. Xu, F. Pan, F. Yuan, J. Dai, B. Jiao, X. Hou, A. K. Y. Jen, Z. Wu, *Sci. Adv.* **2022**, *8*, 2722.
- [4] X. Li, W. Zhang, X. Guo, C. Lu, J. Wei, J. Fang, *Science*. **2022**, *375*, 434.
- [5] R. Wang, M. Mujahid, Y. Duan, Z.-K. Wang, J. Xue, Y. Yang, *Adv. Funct. Mater.* **2019**,

- 29, 1808843.
- [6] A. Kakekhani, R. N. Katti, A. M. Rappe, *APL Mater.* **2019**, 7, 041112.
- [7] Y. Zhou, Y. Zhao, *Energy Environ. Sci.* **2019**, 12, 1495.
- [8] X. Zhao, T. Liu, Y.-L. Loo, *Adv. Mater.* **2022**, 34, 2105849.
- [9] I. C. Smith, E. T. Hoke, D. Solis-Ibarra, M. D. McGehee, H. I. Karunadasa, *Angew. Chemie Int. Ed.* **2014**, 53, 11232.
- [10] I. Zimmermann, E. Mosconi, X. Lee, D. Martineau, S. Narbey, F. Oswald, G. Grancini, C. Rolda, *Nat. Commun.* **2017**, 8, 15684.
- [11] H. Ren, S. Yu, L. Chao, Y. Xia, Y. Sun, S. Zuo, F. Li, T. Niu, Y. Yang, H. Ju, B. Li, H. Du, X. Gao, J. Zhang, J. Wang, L. Zhang, Y. Chen, W. Huang, *Nat. Photonics* **2020**, 14, 154.
- [12] F. Zhang, S. Y. Park, C. Yao, H. Lu, S. P. Dunfield, C. Xiao, S. Uličná, X. Zhao, L. Du Hill, X. Chen, X. Wang, L. E. Mundt, K. H. Stone, L. T. Schelhas, G. Teeter, S. Parkin, E. L. Ratcliff, Y. L. Loo, J. J. Berry, M. C. Beard, Y. Yan, B. W. Larson, K. Zhu, *Science*. **2022**, 375, 71.
- [13] H. Tsai, W. Nie, J. Blancon, C. C. Stoumpos, R. Asadpour, B. Harutyunyan, A. J. Neukirch, R. Verduzco, J. J. Crochet, S. Tretiak, L. Pedesseau, J. Even, M. A. Alam, G. Gupta, J. Lou, P. M. Ajayan, M. J. Bedzyk, M. G. Kanatzidis, A. D. Mohite, *Nature* **2016**, 536, 312.
- [14] L. Mao, W. Ke, L. Pedesseau, Y. Wu, C. Katan, J. Even, M. R. Wasielewski, C. C. Stoumpos, M. G. Kanatzidis, *J. Am. Chem. Soc.* **2018**, 140, 3775.
- [15] N. Zibouche, S. Islam, *ACS Appl. Mater. Interfaces* **2020**, 12, 15328.
- [16] J. Byun, H. Cho, C. Wolf, M. Jang, A. Sadhanala, R. H. Friend, H. Yang, T. Lee, *Adv. Mater.* **2016**, 28, 7515.
- [17] J. Xing, Y. Zhao, M. Askerka, L. N. Quan, X. Gong, W. Zhao, J. Zhao, H. Tan, G. Long, L. Gao, Z. Yang, O. Voznyy, J. Tang, Z.-H. Lu, Q. Xiong, E. H. Sargent, *Nat. Commun.* **2018**, 9, 3541.

- [18] N. Wang, L. Cheng, R. Ge, S. Zhang, Y. Miao, W. Zou, C. Yi, Y. Sun, Y. Cao, R. Yang, Y. Wei, Q. Guo, Y. Ke, M. Yu, Y. Jin, Y. Liu, Q. Ding, D. Di, L. Yang, G. Xing, H. Tian, C. Jin, F. Gao, R. H. Friend, J. Wang, W. Huang, *Nat. Photonics* **2016**, *10*, 699.
- [19] S. Sidhik, Y. Wang, W. Li, H. Zhang, X. Zhong, A. Agrawal, I. Hadar, I. Spanopoulos, A. Mishra, B. Traoré, M. H. K. Samani, C. Katan, A. B. Marciel, J. C. Blancon, J. Even, A. Kahn, M. G. Kanatzidis, A. D. Mohite, *Cell Reports Phys. Sci.* **2021**, *2*, 100601.
- [20] J. L. Knutson, J. D. Martin, D. B. Mitzi, *Inorg. Chem.* **2005**, *44*, 4699.
- [21] K. Z. Du, Q. Tu, X. Zhang, Q. Han, J. Liu, S. Zauscher, D. B. Mitzi, *Inorg. Chem.* **2017**, *56*, 9291.
- [22] X. Li, Y. Fu, L. Pedesseau, P. Guo, S. Cuthriell, I. Hadar, J. Even, C. Katan, C. C. Stoumpos, R. D. Schaller, E. Harel, M. G. Kanatzidis, *J. Am. Chem. Soc.* **2020**, *142*, 11486.
- [23] M. E. Kamminga, H.-H. Fang, M. R. Filip, F. Giustino, J. Baas, G. R. Blake, M. Antonietta Loi, T. T. M. Palstra, *Chem. Mater.* **2016**, *28*, 4554.
- [24] S. Sourisseau, N. Louvain, W. Bi, N. Mercier, D. Rondeau, F. Boucher, J. Y. Buzaré, C. Legein, *Chem. Mater.* **2007**, *19*, 600.
- [25] X. Zhao, M. L. Ball, A. Kakekhani, T. Liu, A. M. Rappe, Y.-L. Loo, *Nat. Commun.* **2022**, *13*, 3970.
- [26] M. L. Ball, J. V. Milić, Y.-L. Loo, *Chem. Mater.* **2022**, *34*, 2495.
- [27] N. Mercier, S. Poiroux, A. Riou, P. Batail, *Inorg. Chem.* **2004**, *43*, 8361.
- [28] N. Ashari-Astani, F. Jahanbakhshi, M. Mladenović, A. Q. M. Alanazi, I. Ahmadabadi, M. R. Ejtehadi, M. I. Dar, M. Grätzel, U. Rothlisberger, *J. Phys. Chem. Lett.* **2019**, *10*, 3543.
- [29] N. Mercier, N. Louvain, W. Bi, *CrystEngComm* **2009**, *11*, 720.
- [30] N. Mercier, *CrystEngComm* **2005**, *7*, 429.
- [31] S. Silver, J. Yin, H. Li, J. L. Brédas, A. Kahn, *Adv. Energy Mater.* **2018**, *8*, 1703468.
- [32] X. Zhong, X. Ni, S. Sidhik, H. Li, A. D. Mohite, J. Brédas, A. Kahn, *Adv. Energy Mater.*

- 2022**, *12*, 2202333.
- [33] S. Silver, S. Xun, H. Li, J. Brédas, A. Kahn, *Adv. Energy Mater.* **2020**, *10*, 1903900.
- [34] Y. Shao, W. Gao, H. Yan, R. Li, I. Abdelwahab, X. Chi, L. Rogée, L. Zhuang, W. Fu, S. P. Lau, S. F. Yu, Y. Cai, K. P. Loh, K. Leng, *Nat. Commun.* **2022**, *13*, 1.
- [35] R. J. Elliott, *Phys. Rev.* **1957**, *108*, 1384.
- [36] S. Yu, J. Xu, X. Shang, E. Ma, F. Lin, W. Zheng, D. Tu, R. Li, X. Chen, *Adv. Sci.* **2021**, *8*, 1.
- [37] L. Ni, U. Huynh, A. Cheminal, T. H. Thomas, R. Shivanna, T. F. Hinrichsen, S. Ahmad, A. Sadhanala, A. Rao, *ACS Nano* **2017**, *11*, 10834.
- [38] S. G. Motti, M. Kober-Czerny, M. Righetto, P. Holzhey, J. Smith, H. Kraus, H. J. Snaith, M. B. Johnston, L. M. Herz, *Adv. Funct. Mater.* **2023**, 2300363
- [39] E. R. Dohner, A. Jaffe, L. R. Bradshaw, H. I. Karunadasa, *J. Am. Chem. Soc.* **2014**, *136*, 13154.
- [40] M. C. Gélvez-Rueda, S. Peeters, P. C. Wang, K. M. Felter, F. C. Grozema, *Helv. Chim. Acta* **2020**, *103*, 14.
- [41] J. Endres, D. A. Egger, M. Kulbak, R. A. Kerner, L. Zhao, S. H. Silver, G. Hodes, B. P. Rand, D. Cahen, L. Kronik, A. Kahn, *J. Phys. Chem. Lett.* **2016**, *7*, 2722.
- [42] F. Zhang, J. C. Hamill, Y. L. Loo, A. Kahn, *Adv. Mater.* **2020**, 2003482, 1.
- [43] A. M. Boehm, T. Liu, S. M. Park, A. Abtahi, K. R. Graham, *ACS Appl. Mater. Interfaces* **2020**, *12*, 5209.
- [44] S. M. Park, A. Abtahi, A. M. Boehm, K. R. Graham, *ACS Energy Lett.* **2020**, *5*, 799.
- [45] R. Quintero-bermudez, A. H. Proppe, A. Mahata, P. Todorovic, S. O. Kelley, F. De Angelis, E. H. Sargent, *J. Am. Chem. Soc.* **2019**, *141*, 13459.
- [46] K. R. Hansen, C. Y. Wong, C. E. McClure, B. Romrell, L. Flannery, D. Powell, K. Garden, A. Berzansky, M. Eggleston, D. J. King, C. M. Shirley, M. C. Beard, W. Nie, A. Schleife, J. S. Colton, L. Whittaker-Brooks, *Matter* **2023**, *6*, 3463.

- [47] J. Heyd, G. E. Scuseria, M. Ernzerhof, *J. Chem. Phys.* **2003**, *118*, 8207.
- [48] B. Cheng, T. Y. Li, P. Maity, P. C. Wei, D. Nordlund, K. T. Ho, D. H. Lien, C. H. Lin, R. Z. Liang, X. Miao, I. A. Ajia, J. Yin, D. Sokaras, A. Javey, I. S. Roqan, O. F. Mohammed, J. H. He, *Commun. Phys.* **2018**, *1*, 80.
- [49] T. Ishihara, J. Takahashi, T. Goto, *Solid State Commun.* **1989**, *69*, 933.
- [50] R. Chakraborty, A. Nag, *J. Phys. Chem. C* **2020**, *124*, 16177.
- [51] M. R. Filip, D. Y. Qiu, M. Del Ben, J. B. Neaton, *Nano Lett.* **2022**, *22*, 4870.
- [52] E. A. Muljarov, S. G. Tikhodeev, N. A. Gippius, T. Ishihara, *Phys. Rev. B* **1995**, *51*, 14370.
- [53] G. Kresse, J. Furthmuller, *Phys. Rev. B* **1996**, *54*, 11169.
- [54] J. P. Perdew, K. Burke, M. Ernzerhof, *Phys. Rev. Lett.* **1996**, *77*, 3865.
- [55] J. P. Perdew, K. Burke, M. Ernzerhof, *Phys. Rev. Lett.* **1997**, *78*, 1396.
- [56] S. Grimme, J. Antony, S. Ehrlich, H. Krieg, *J. Chem. Phys.* **2010**, *132*, 154104.
- [57] A. V Krukau, O. A. Vydrov, A. F. Izmaylov, G. E. Scuseria, *J. Chem. Phys.* **2006**, *125*, 224106.